



Formation of Fe–Mn–Si oxide and nontronite deposits in hydrothermal fields on the Valu Fa Ridge, Lau Basin

Zhilei Sun^{a,b}, Huaiyang Zhou^{c,*}, G.P. Glasby^{a,b}, Qunhui Yang^c, Xijie Yin^d, Jiwei Li^e, Zhiqiang Chen^f

^a Key Laboratory of Marine Hydrocarbon Resources and Environmental Geology, Ministry of Land and Resources, Qingdao 266071, China

^b Qingdao Institute of Marine Geology, Qingdao 266071, China

^c State Key Laboratory of Marine Geology, Tongji University, Shanghai 200092, China

^d Third Institute of Oceanography State Oceanic Administration, Xiamen 361000, China

^e Southwest Jiaotong University, Chengdu 610031, China

^f Guangzhou Institute of Geochemistry, Chinese Academy of Sciences, Guangzhou 510640, China

ARTICLE INFO

Article history:

Received 20 November 2010

Received in revised form 12 August 2011

Accepted 17 August 2011

Available online 13 September 2011

Keywords:

Valu Fa Ridge

Hydrothermal vent

Fe–Mn–Si oxides

Nontronite

Neutrophilic Fe-oxidizing bacteria

ABSTRACT

Hydrothermal Fe–Mn–Si oxides and nontronite are pervasive in the Hine Hina, Vai Lili and Mariner hydrothermal fields along the central Valu Fa Ridge, Lau Basin. Morphometric and mineralogical analyses reveal that the iron-rich filaments are the most important constituents of these Fe–Mn–Si oxide deposits. Both the morphologies and chemical composition of the filaments indicate that neutrophilic Fe-oxidizing bacteria have played a key role in the formation of these deposits. A key process of the formation of these deposits is the creation of a complicated filamentous network in which a series of metabolic activities and passive sorption and nucleation processes occur. The precipitation of dissolved Si in unsaturated and saturated states leads to a “two-generation” growth model in the hydrothermal vents. The precipitation of amorphous opal occurs in a relatively narrow temperature range (41.1–42.9 °C) based on oxygen isotope analyses, indicating a fast precipitation rate of opal-A when conductive cooling of the hydrothermal fluid occurs. Patchy nontronite in the Mariner fields is a product of the direct precipitation from hydrothermal fluids at a temperature of ~87.9 °C, whereas the scattered nontronite at the Hine Hina field is the product of the replacement of hydrothermal Fe–Si oxides at a temperature of ~46.2 °C.

© 2011 Elsevier Ltd. All rights reserved.

1. Introduction

Poorly crystallized Fe–Mn–Si-oxyhydroxide deposits (referred to as Fe–Mn–Si oxides) are widely developed in modern hydrothermal fields in various geological settings, such as mid-ocean ridges, back-arc basins and intra-plate seamounts (e.g., Alt, 1988; Puteanus et al., 1991; Binns et al., 1993; Fortin et al., 1998; Iizasa et al., 1998; Boyd and Scott, 2001; Kennedy et al., 2003a,b; Benjamin and Haymon, 2006; Hrischeva and Scott, 2007; Kato et al., 2009; Langley et al., 2009; Dekov et al., 2010; Edwards et al., 2011). Mineralogically, these hydrothermal precipitates contain a wide range of minerals with primary ferrihydrite, goethite, amorphous silica (opal-A), todorokite, birnessite and sometimes Fe-rich phyllosilicates such as nontronite (Köhler et al., 1994; Iizasa et al., 1998; Benjamin and Haymon, 2006; Hrischeva and Scott, 2007) and Fe-rich smectite present (Cole, 1983, 1985, 1988; Taitel-Goldman and Singer, 2001a,b).

* Corresponding author at: State Key Laboratory of Marine Geology, Tongji University, Shanghai 200092, China. Tel.: +86 21 65987961; fax: +86 21 65983385 (H. Zhou).

E-mail address: zhouhy@tongji.edu.cn (H. Zhou).

In recent years, there has been considerable interest in understanding the formation of Fe–Mn–Si oxides (especially Fe-oxyhydroxides) in seafloor hydrothermal fields. An important reason for this is that mineralized bacterial micro-textures (filaments and spheres) are ubiquitous in these deposits (e.g., Taylor et al., 1999; Emerson and Moyer, 2002; Kennedy et al., 2003a,b; Little et al., 2004; Emerson et al., 2007; Kato et al., 2009; Langley et al., 2009; Dekov et al., 2010; Edwards et al., 2011). So far, several studies based on the morphologies of the filaments and molecular biological techniques have revealed the presence of neutrophilic Fe-oxidizing bacteria (i.e., *Gallionella ferruginea*, *Leptothrix ochracea* and *Mariprofundus ferrooxydans*) in hydrothermal vent systems (Dhillon et al., 2003; Emerson et al., 2007, 2010; Davis and Moyer, 2008; Hodges and Olson, 2009; Kato et al., 2009), suggesting that bacteria play an important role in the formation of the hydrothermal Fe–Mn–Si oxide deposits. In addition, more and more researches have shown that these deposits are probably the analogs of ancient banded iron formations (BIFs) and umbers (Boyd and Scott, 2001; Pecoits et al., 2009; Edwards et al., 2011). Similar biogenic filamentous structures have also been discovered in similar ancient deposits (Duhig et al., 1992; Boyce et al., 2003). Some recent studies have demonstrated that the unique morphologies

of neutrophilic Fe-oxidizing bacteria can act as robust biosignatures for the investigation of the evolution of life and for geological studies (Hofmann et al., 2008; Chan et al., 2011). In order to create a closer affinity to similar ancient deposits, this demands further thorough investigations focused on the formation of Fe–Si–Mn oxide deposits in modern hydrothermal fields. However, understanding the processes of Fe–Mn–Si oxide precipitation and the role of bacteria in seafloor hydrothermal fields still remains limited at present (Kato et al., 2009; Langley et al., 2009; Emerson et al., 2010).

Furthermore, as a common authigenic clay mineral, nontronite generally occurs in modern hydrothermal deposits intermixed with the Fe–Mn–Si oxide (Severmann et al., 2004; Dekov et al., 2007) reflecting the variable redox conditions over short distances (Severmann et al., 2004). Previous studies have revealed that nontronite can form at temperatures of 3–140 °C (Benjamin and Haymon, 2006) and various formation mechanisms for this have been proposed (Cole and Shaw, 1983; Severmann et al., 2004; Benjamin and Haymon, 2006; Benjamin and Haymon, 2006; Dekov et al., 2007) including weathering/alteration of massive sulfides, metalliferous sediments and oceanic crust (McMurtry and Yeh, 1981; Haymon and Kastner, 1986; Hekinian et al., 1993) and the direct precipitation of nontronite from low-temperature hydrothermal fluids (McMurtry et al., 1983; Alt and Jiang, 1991; Percival and Ames, 1993; Severmann et al., 2004). Moreover, several studies suggest a biogenic origin for hydrothermal nontronite and have described bacterial structures associated with this mineral (Alt, 1988; Juniper and Fouquet, 1988; Hekinian et al., 1993; Köhler et al., 1994; Fortin et al., 1998; Dekov et al., 2007). However, the relationship between Fe–Mn–Si oxides and nontronite during their precipitation in hydrothermal vents is not well established (Severmann et al., 2004).

In this paper, we present a preliminary study of the mineralogy, geochemistry and morphology of Fe–Mn–Si oxide and nontronite precipitates from hydrothermal fields on the southern and central Valu Fa Ridge (VFR), Lau Basin. The main objectives of this study were to determine the mechanism of formation of these precipitates

and the role of microbes in the formation of the hydrothermal Fe–Mn–Si oxides.

2. Geological setting

The Lau Basin is located at a convergent boundary between the Pacific and Indo-Australian plates and is approximately 1500 km north of New Zealand. Below 1000 m it is largely closed to the east, south and west by a remnant arc (Lau Ridge) and an active volcanic arc (Tofua volcanic arc), respectively (Fig. 1) (Fouquet et al., 1993; Keller et al., 2008). The basin is composed of three major active spreading ridges: the Central Lau Spreading Center (CLSC), the Eastern Lau Spreading Center (ELSC), and the southernmost part of the ridge (21°20'S), which is referred to as the Valu Fa Ridge (VFR) (Jenner et al., 1987). This active back-arc basin has been opening over the past 6 Ma (Hawkins, 1995) whereas the Valu Fa spreading ridge (the southern part of the Lau Basin) began opening about one Ma ago (Lécuyer et al., 1999). The VFR extends for at least 165 km and is 5–6 km wide with the ridge flanks rising about 600 m above the surrounding seafloor (Taylor et al., 1996). Geophysical studies suggest that the VFR is divided into three sections: the southern, central and northern VFR (SVFR, CVFR and NVFR) sections (Fouquet et al., 1993), which are arranged *en echelon* a few kilometers apart. The southern Valu Fa Ridge is still propagating southwards.

Since the early 1990s, several distinct hydrothermal fields have been discovered along the VFR extensional zone (Fouquet et al., 1991, 1993; Ishibashi et al., 2006; Reysenbach et al., 2006). According to Fouquet et al. (1993), two different volcanic and tectonic stages have been recognized in the SVFR and NVFR. The Hine Hina hydrothermal field on the SVFR is in the volcanic stage and is characterized by diffuse discharge at ~40 °C (Fouquet et al., 1993; Lécuyer et al., 1999; Baker et al., 2005) through highly porous volcanoclastic material which was produced during the formation of extensive Fe–Mn-oxyhydroxide crusts covering sulfide

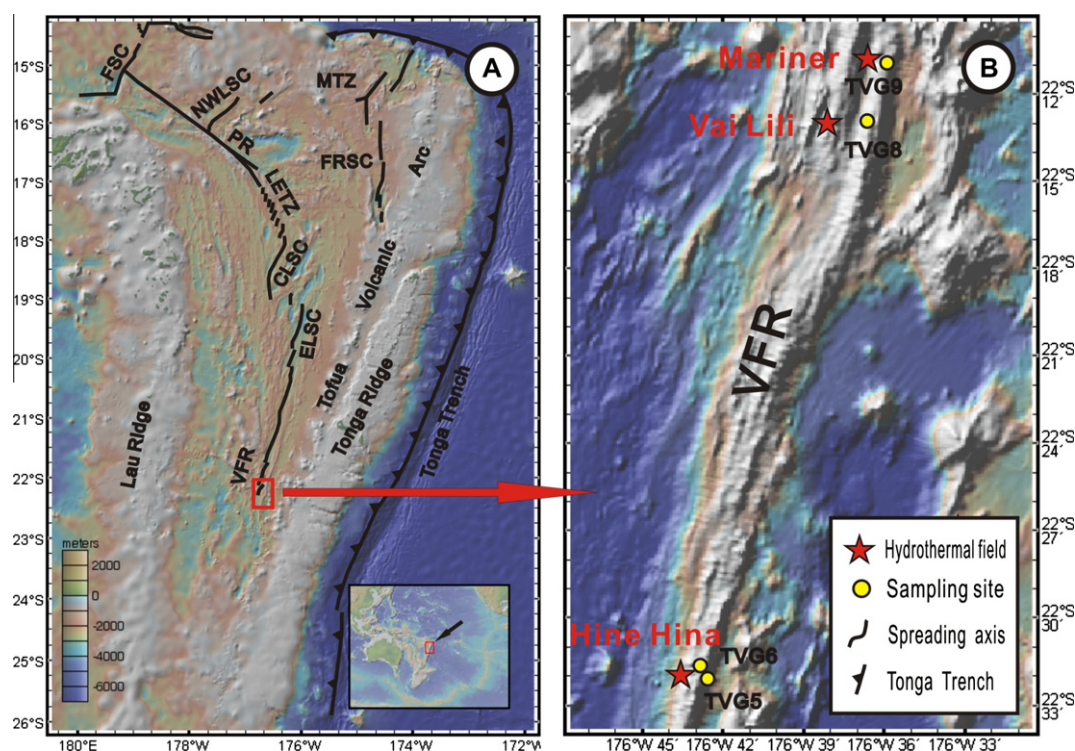


Fig. 1. Regional bathymetric map and the sample sites along the VFR, Lau Basin. Red stars = hydrothermal vent sites; yellow circles = sampling sites.

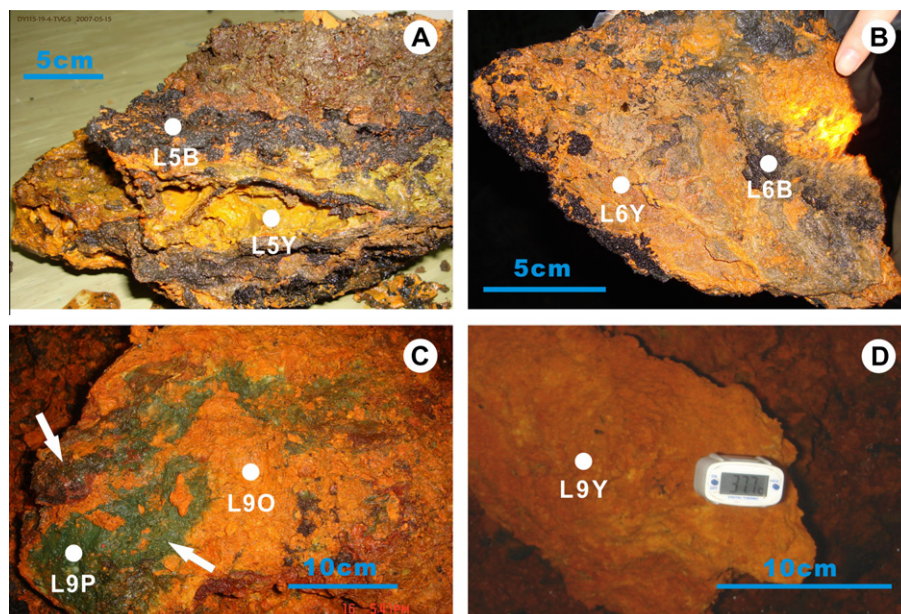


Fig. 2. Fe–Mn–Si oxides and patchy nontronite from the VFR. The corresponding sample sites are indicated by white points on the photographs. (A) Fe–Mn oxide crusts from the Hine Hina hydrothermal field showing laminated structures, TVG5 station. (B) Fe–Mn oxide crusts from the Hine Hina hydrothermal field showing laminated structures, TVG6 station. (C) Fe–Si oxides with patchy nontronite (white arrows) from the Mariner field. (D) Photograph of Fe–Si oxides in the Mariner field, TVG9 station. The thermometer shows that the immediate temperature of the deposits was 37.7 °C when they were brought on deck in the TV-guided grab.

deposits within the volcanic material (Fouquet et al., 1993; Lécuyer et al., 1999). The Vai Lili and Mariner fields were discovered on the CVFR (Fouquet et al., 1991; Baker et al., 2005, 2006; Martinez et al., 2006) and are now at the volcanic/tectonic stage. At these two fields, there are numerous black and white smokers discharging fluids with temperatures up to 400 °C at Vai Lili field and up to ~365 °C at the Mariner field (Takai et al., 2008). In addition, diffuse discharges depositing Fe–Mn oxides are also present in this area (Lécuyer et al., 1999). The White Church field (not shown in Fig. 1) in the northern portion VFR is at the tectonic stage but there is no evidence of widespread Fe–Mn oxide deposits (Fouquet et al., 1993; Lécuyer et al., 1999) except for the presence of numerous barite chimneys and small Mn-oxide chimneys controlled by major faults (Lécuyer et al., 1999).

3. Materials and methods

3.1. Sampling and sample descriptions

Several Fe–Mn–Si oxide samples were recovered using a TV-guided Grab (TVG) at the Hine Hina (TVG5, TVG6), the Vai Lili (TVG8), and the Mariner (TVG9) hydrothermal fields along the southern and central VFR during the cruise of R/V *DaYang One* in May 2007 (Fig. 1B). The samples from the TVG5 and TVG6 stations were semi-consolidated, slightly laminated and coated with a thin film of crusts (on a mm to cm scale) of sooty, black material containing abundant volcanic glass shards which were used in this study. Two samples named L5Y and L6Y were taken from each yellow¹ layer of TVG5 and TVG6 and two samples named L5B and L6B were taken from each of the black layer of TVG5 and TVG6 (Fig. 2A and B). The TVG8 and TVG9 samples did not display any laminated textures and were mainly bright yellow to orange yellow with some greenish patches (Fig. 2C, as the arrowhead indicates). One sample named L8Y was taken from TVG8 (not shown in Fig. 2) and two samples named L9O and L9Y were taken from TVG9 (Fig. 2C and D). Furthermore, the green patchy sample named

L9P was also taken from TVG9 (Fig. 2C). Detailed information and the nomenclature of all the samples are given in Table 1.

It is noteworthy that the maximum temperature of the TVG9 sample was 37.7 °C recorded 10 min after recovery of the sample on deck (Fig. 2D). This demonstrates that the sample was taken from an active hydrothermal vent.

3.2. Analytical methods

After freeze-drying, two samples from TVG5 and TVG6 respectively were first reacted with 1 N sodium acetate buffer (pH = 5) to remove carbonate minerals and then with 30% H₂O₂ to remove organic matter and manganese oxides (Jackson, 1985). The rest of the sample was treated with citrate-dithionite (CD) to get rid of any Fe oxides (Coffin, 1963) and the <2 μm fraction was separated by the standard Stokes method (Pansu and Gautheyrou, 2006). Altogether 1.47 g of clay-fraction mineral (named L5S) was extracted from 121.1 g dry oxides in the bulk TVG5 sample with a content of 1.21 wt.%. By contrast, we could not obtain enough clay-fraction minerals from the sample of TVG6 (54.3 g dry samples) for study.

In addition, two samples from TVG9 (L9O and L9Y) were purified to remove carbonates and organic matter and the Fe–Mn oxides according to the treatment procedure mentioned above in order to obtain pure silica samples for oxygen isotope analysis. The oxygen isotopic compositions of the four samples (L5S, L9P, L9O, and L9Y) were determined on CO₂ generated from silicates using the BrF₅ technique (Clayton and Mayeda, 1963) performed on a MAT 253 mass spectrometer at the Institute of Mineral Resources of the Chinese Academy of Geological Sciences, Beijing. All these analyses have been fully duplicated (including different aliquots, chemical separation and spectrometric determinations). The analytical data were reported on a per mil (‰) scale relative to Vienna Standard Mean Ocean Water (VSMOW) with a typical error on a δ¹⁸O determination of approximately ±0.1‰.

The mineralogy of the samples was investigated by X-ray Diffraction (XRD) with a D/max2550VB3+/PC diffractometer (operating at 35 kV and 30 mA) using Cu Kα radiation with a scan rate of 1° per minute and a 2θ range from 2.5° to 80°. Optical microscopy

¹ For interpretation of color in Figs. 1, 2, 5–9, the reader is referred to the web version of this article.

Table 1

Description of the hydrothermal Fe–Mn–Si oxides and phyllosilicates from the VFR, Lau Basin.

| Field | Sample | TVG No. | Lat. (S) | Long. (W) | Depth (m) | Description | Mineral composition ^a |
|-----------|--------|---------|-----------|------------|-----------|---|----------------------------------|
| Hine Hina | L5B | 5 | 22°32′01″ | 176°42′39″ | 1906 | Sooty, layered, semi-consolidated | B, V, Sa |
| Hine Hina | L5Y | 5 | 22°32′01″ | 176°42′39″ | 1906 | Yellow, layered, semi-consolidated | Op, Fh |
| Hine Hina | L5S | 5 | 22°32′01″ | 176°42′39″ | 1906 | Clay fraction (<2 μm , after purification) | N |
| Hine Hina | L6B | 6 | 22°31′54″ | 176°42′56″ | 1877 | Black, layered, semi-consolidated | B, V, Sa |
| Hine Hina | L6Y | 6 | 22°31′54″ | 176°42′56″ | 1877 | Yellow, layered, semi-consolidated | Op, Fh |
| Vai Lili | L8Y | 8 | 22°12′57″ | 176°36′26″ | 1744 | Yellow–brown, massive | Fh, Op, Py, Sph |
| Mariner | L9O | 9 | 22°10′53″ | 176°36′06″ | 1922 | Orange yellow, massive, loose | Op, Fh |
| Mariner | L9Y | 9 | 22°10′53″ | 176°36′06″ | 1922 | Bright yellow, massive, loose | Op, Fh |
| Mariner | L9P | 9 | 22°10′53″ | 176°36′06″ | 1922 | Greenish, patchy | N |

^a (1) B = birnessite, V = vernadite, Sa = saponite, Op = amorphous opal, Fh = 2-line-ferrihydrite, Py = pyrite, Sph = sphalerite, N = nontronite; (2) The last alphabet “Y” of the sample name indicates that the sample is yellow, the “B” is black, the “O” is orange and the “P” indicates that the sample has a patchy appearance; (3) Analytical methods: XRD, Mössbauer Spectroscopy.

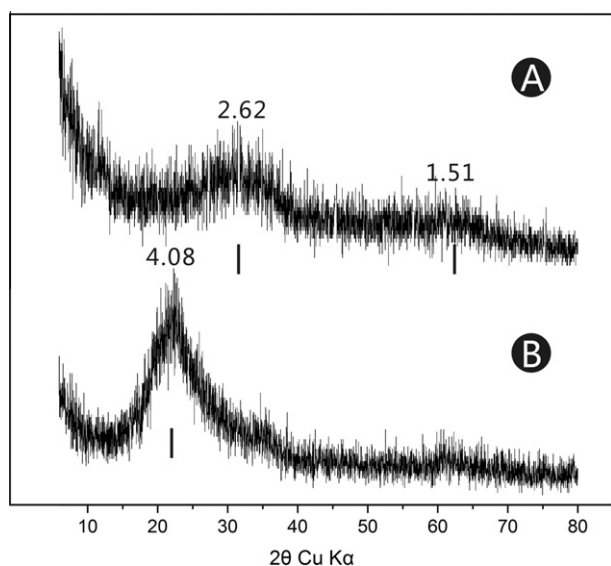


Fig. 3. Selected XRD patterns of Fe–Si oxide deposits on the VFR, the numbers represent d-spacing in Ångströms. (A) 2-line-ferrihydrite showing two main humps at the centers with spacings of $d = 2.62$ Å and $d = 1.51$ Å, respectively, sample L5Y. (B) amorphous opal showing a main hump at the center with a spacing of $d = 4.08$ Å, sample L9O.

was used to identify trace minerals and amorphous phases which could not be detected by XRD analysis. Petrographic relationships were observed in thin section using an optical microscope with both reflected and transmitted light.

All the samples were hand-picked and freeze-dried and small (~1 cm in diameter) pieces of these samples were selected for scanning electron microscopy. SEM observations were carried out on C-coated fragments of freeze-dried bulk samples using a FEI Quant 400 electron microscope with an accelerating voltage of 15 keV. Semi-quantitative chemical analyses were undertaken using an energy dispersion X-ray Analyzer with an accelerating voltage of 20 keV for 100 s.

In order to investigate the compositions of the filaments on a fine scale, an Electron Probe Micro-analyzer (EPMA) equipped with an energy-dispersive spectrometer (EDS) was used for the chemical analysis. Altogether six samples (L5Y, L6Y, L8Y, L9O, L9Y and L9P) were chose for EPMA because they contained abundant filaments as observed by optical microscopy. All the samples were embedded in epoxy resin, mounted on pure quartz slides and polished to 30 μm thickness to form thin sections and were sputter coated with carbon prior to microprobe analysis. Particles of interest were identified by EDS screening. All these analyses above were carried out at Tongji University, Shanghai.

⁵⁷Fe Mössbauer spectroscopy was performed on six powdered samples (L5B, L5Y, L6B, L6Y, L9Y and L9P) using conventional

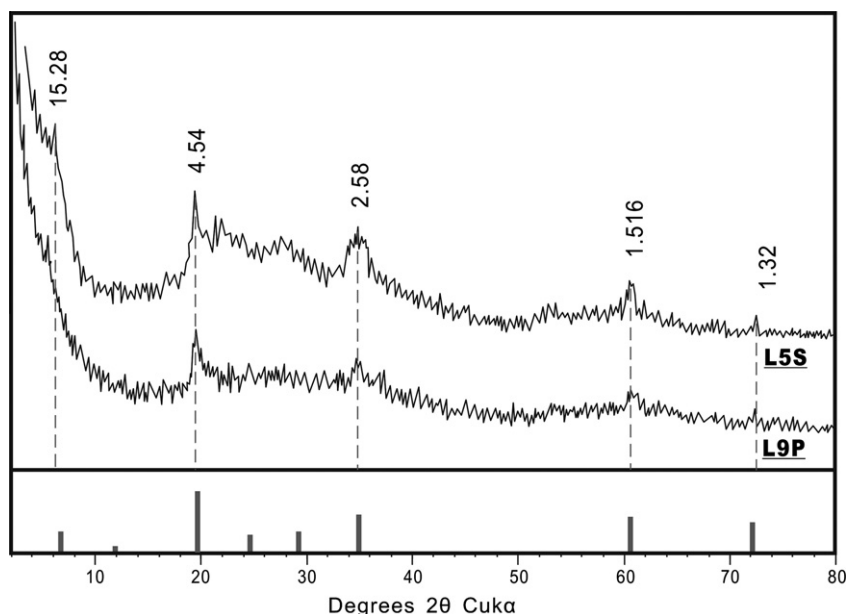


Fig. 4. XRD patterns of nontronite on the VFR, sample L5S and L9P. The numbers represent d-spacing in Ångströms and the sample names are marked by underlining. Relative peak intensities (vertical lines along x-axis) for nontronite (PDF#29–1497) are taken from the MDI Jade 5.0 platform.

Mössbauer spectroscopy (Wissel) in transmission geometry at room temperature (RT) at the School of Physics of Nanjing University. A $^{57}\text{Co}/\text{Rh}$ γ -radiation source of 3.6×10^9 Bq activity was used and the isomer shifts were reported relative to α -Fe. The Mössbauer source was driven at constant acceleration between -4.0 and $+4.0$ mm s $^{-1}$. The resulting Mössbauer spectra

were fitted with doublets of Lorentzian peaks using a sum of squares minimization algorithm in a platform of the Mosswin 3.0 code. The intensities of the two peaks in each doublet were constrained to have an equal area and shape. Each doublet within a Mössbauer spectrum corresponded to a distinct iron site within the sample.

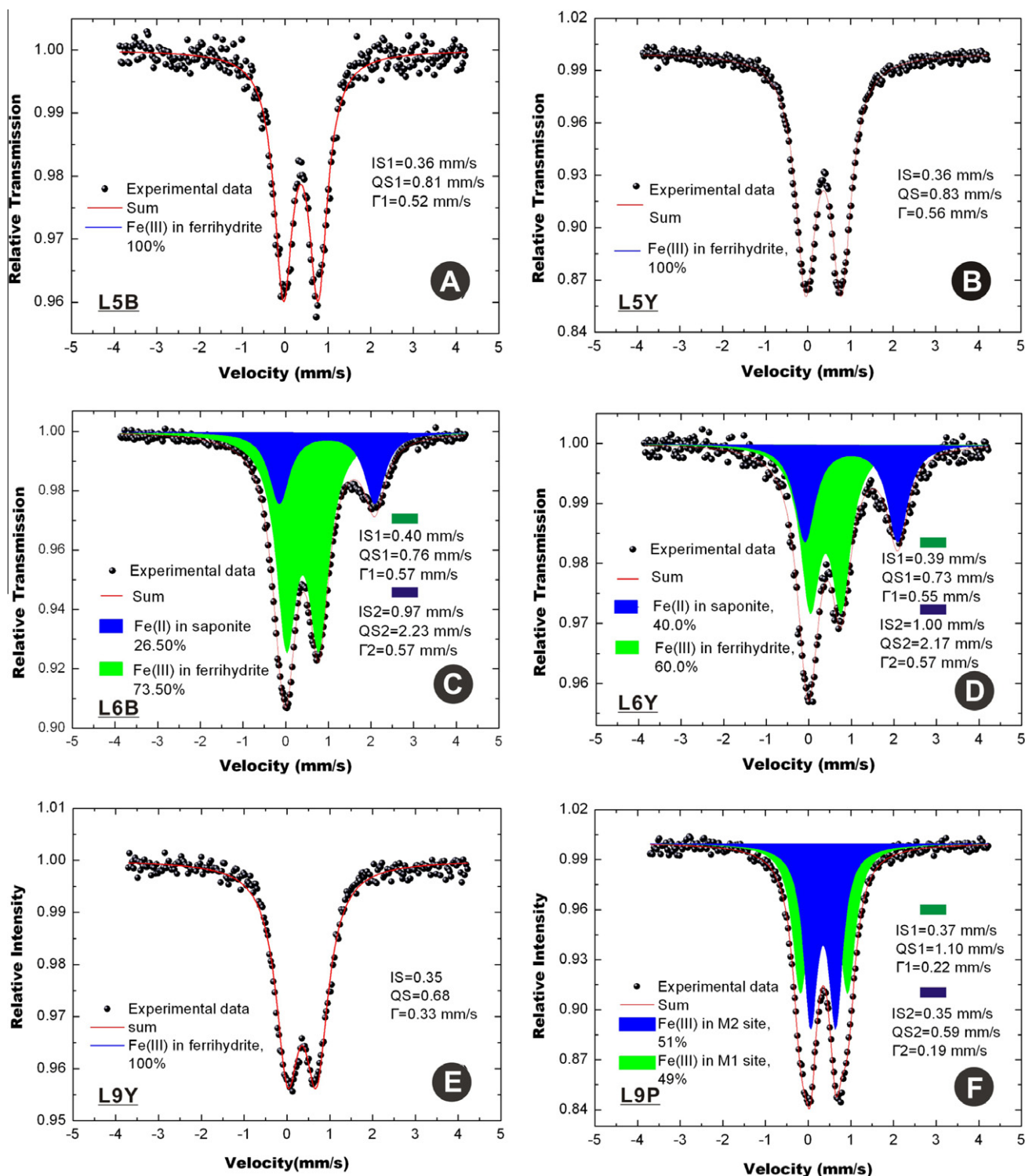


Fig. 5. ^{57}Fe Mössbauer spectra (room temperature) and fitting results of the hydrothermal Fe–Si–Mn oxide deposits on the VFR. The sample numbers and corresponding analytical results are listed in Table 2. In every sub-picture, brief results are listed to the left and parameters to the right.

4. Results

4.1. Mineralogy

The mineralogical results of all the nine samples distinguished by color are summarized in Table 1. The blackish-layered samples (L5B, L6B) are principally composed of birnessite with minor vernadite (δ -MnO₂). The XRD patterns of yellow samples (L5Y, L6Y, L8Y) were characterized by similar XRD patterns (Fig. 3A) with weak humps near $d = 2.62$ Å and 1.51 Å, which are typical of poorly crystalline 2-line-ferrihydrite (Jambor and Dutrizac, 1998). Some orange-bright yellow samples (L9O and L9Y) show a broad, diffuse peak centred at about 4.08 Å (Fig. 3B), which is typical for amorphous silica (opal-A, SiO₂·nH₂O) according to the nomenclature of Jones and Segnit (1971, 1975) and Herzig et al. (1988). The clay fraction mineral L5S and the green patchy sample (L9P) have very similar XRD patterns, which indicates that these sample are dominated by pure smectite (Fig. 4). The $d_{(060)}$ equals 1.516 Å and reveals that these smectites are dioctahedral (Wilson, 1987). It is worth noting that there is no patchy or layered smectite in the Hine Hina field and clay minerals there were found scattered in Fe–Mn–Si oxides at low concentrations (1.21 wt.%) as stated in Section 3.2.

Mössbauer investigations of the samples revealed three types of spectra (Fig. 5; Table 2). The spectra of the L5B, L5Y were fitted by means of a single Lorentzian doublet. Parameters of IS (isomer shift, 0.36 mm/s) and QS (quadrupole splitting, 0.81–0.83 mm/s) (Fig. 5A and B) hinted that the doublet could be ascribed to a high-spin Fe(III) state. According to previous studies (e.g., Murad and Schwertmann, 1980; Rancourt et al., 2001; Mikutta et al., 2008; Langley et al., 2009), these parameters of the Mössbauer spectra confirm the presence of 2-line-ferrihydrite which is consistent with the XRD analyses. The Mössbauer spectra of L6B and L6Y were fitted by two different Lorentzian doublets (Fig. 5C and D). The narrower doublet had a higher IS (0.39–0.40 mm/s) and QS (0.73–0.76 mm/s) and was related to the octahedrally-coordinated Fe(III) which occurs as 2-line-ferrihydrite. The broader doublet (IS = 0.97–1.00 mm/s, QS = 2.17–2.23 mm/s) is typical of paramagnetic high-spin Fe(II) in 2:1 clay minerals in which Fe(II) occupies the M1 (trans-) site (Fig. 5E and F). Based on the previous work (Sherman and Vergo, 1988), the 2:1 clay mineral was shown to be Fe-bearing saponite. The yellowish sample L9P (Fig. 5E) showed a very similar result to L5B and L5Y (IS = 0.35 mm/s, QS = 0.68 mm/s) suggesting that the main component of this sample is ferrihydrite. The green patchy sample (L9P) and clay-sized fraction (L5S) displayed another type of Mössbauer spectra fitted with two Lorentzian doublets (Fig. 5F). The outer doublet (IS = 0.37 mm/s, QS = 1.10 mm/s) indicates that Fe(III) occupies the M1 site in the octahedral site in the inner doublet (IS = 0.35 mm/s, QS = 0.59 mm/s) and is representative of Fe(III) in the octahedral site as well. The rather small QS reflects the moderate distortion of the octahedral site. As a result, this inner doublet occupies the M2 site. Based on the previously mentioned parameters and the XRD patterns (Fig. 4), this mineral was therefore shown to be nontronite.

4.2. Microtextures, micromorphologies and compositions

Optical microscopy and SEM observations revealed that birnessite in the black samples typically occurs as tiny rosettes (Fig. 6A) with the main components O, Mn and Na as the EDS results show (Fig. 6H). Pure opal-A occurs in some yellow samples as aggregates with smooth globular or spheroidal morphologies (Fig. 6B and I). Filamentous structures are the most abundant in the yellow deposits (Fig. 6C and D). It is interesting that filaments with short

Table 2

Mössbauer parameters of Fe–Mn–Si deposits on the VFR at room temperature.

| Sample | χ^2 | A (%) | IS (mm/s) | QS (mm/s) | LW (mm/s) | Assignment |
|--------|----------|-------|-----------|-----------|-----------|-----------------------|
| L5B | 1.69 | 100 | 0.36(6) | 0.81(2) | 0.52(1) | Fe ³⁺ |
| L5Y | 2.92 | 100 | 0.36(7) | 0.83(7) | 0.56(1) | Fe ³⁺ |
| L6Y | 1.52 | 60 | 0.39(5) | 0.73(0) | 0.55(4) | Fe ³⁺ (M2) |
| | | 40 | 1.00(0) | 2.17(7) | 0.57(5) | Fe ²⁺ (M1) |
| L6B | 2.56 | 73.5 | 0.40(0) | 0.76(1) | 0.57(9) | Fe ³⁺ (M2) |
| | | 26.5 | 0.97(1) | 2.23(9) | 0.57(5) | Fe ²⁺ (M1) |
| L9Y | 3.97 | 100 | 0.35(3) | 0.68(9) | 0.33(8) | Fe ³⁺ |
| L9P | 1.59 | 49.5 | 0.37(8) | 1.10(7) | 0.22(4) | Fe ³⁺ (M1) |
| | | 50.5 | 0.35(1) | 0.59(0) | 0.19(5) | Fe ³⁺ (M2) |

A = relative spectral area; IS = isomer shift; QS = quadrupole splitting; LW = Full width at half maximum; Errors (in parentheses) are in scientific notation, e.g., 1.56(6) = 1.56 ± 0.006 .

rod-like and oval appearances contain less Fe (Fig. 6J) than filaments with slim threadlike appearances (Fig. 6K). Furthermore, the threadlike filaments also contain significant amounts of P, Cl and Na (Fig. 6K). The green patchy phyllosilicate in the Mariner field displays a honeycomb texture (Fig. 6E) whereas the irregular phyllosilicates in the Hine Hina field commonly grow perpendicular to the Fe–Si oxides substrates based on SEM observations (Fig. 6F and G). As shown in the EDS results, the phyllosilicates also contain significant amounts of O, Si, Fe, Mn and Na and minor amounts of C (Fig. 6L) confirming that it is nontronite.

Based on thin section and SEM observation, a yellow mineral phase forms alteration rinds around the included basalt clasts and is present at the edges of glass shards (Fig. 7A and B). This mineral has the appearance of a cryptocrystalline phyllosilicate and has a greenish-yellow color in cross-polarized light (Fig. 7A). Yellow staining from oxidized Fe-minerals also probably augments the strong coloration of the phyllosilicate minerals. The EPMA results show that the alteration products all contain a major amount of O, Si, Fe, Ca, Mg (Fig. 7C and D). At one detection point, a significant amount of Mn and a minor amount of Al was also detected (Fig. 7C). Since there is no phyllosilicate identified by Mössbauer spectral (MS) analysis apart from saponite, we think the main breakdown products of the basaltic debris are Fe-bearing saponite. We did not observe any saponite reflections in the XRD patterns probably because saponite occurs in minor phases and/or in poorly crystalline phases in the bulk samples (Zee et al., 2005).

As shown in Fig. 8, the yellow samples (L5Y, L6Y, L8Y and L9Y) are composed mainly of Fe–Si oxides and display filamentous structures. According to previous studies (e.g., Emerson and Moyer, 2002; Kennedy et al., 2003a,b; Little et al., 2004; Emerson et al., 2007), three types of filaments could be identified in our samples by means of SEM and optical microscopy. The ribbon-like helical structure of the filaments (Fig. 8A and B) resembles that in the newly discovered iron oxidizing bacterium *M. ferrooxydans* (PV-1 strain) whereas the distinctive twisted structure (Fig. 8C and D) was similar to the stalk of *G. ferruginea*, and the straight rod-like structure (Fig. 8E and F) to that of the sheath of *L. ochracea*. In their initial stage of formation, these filaments are 1–10 µm in diameter, up to several hundred microns in length and sometimes display tiny spheroidal blebs on their surfaces (Fig. 8A). We noted that these filaments often evolve into loose networks, some of which are interlocked with each other and form a mesh structure (Fig. 8G and H), some of which radiates out from a central mass (Fig. 8I and J) and some of which are orientated roughly parallel to the laminae (Fig. 8K). All these structures have abundant voids within them but, in some samples which have experienced silicification, these voids or meshes are filled with pure silica and the loose mats have become dense crusts (Fig. 8L).

Quantitative elemental analysis (acquired by EPMA) corroborates the process described above (Fig. 9). The composition of the

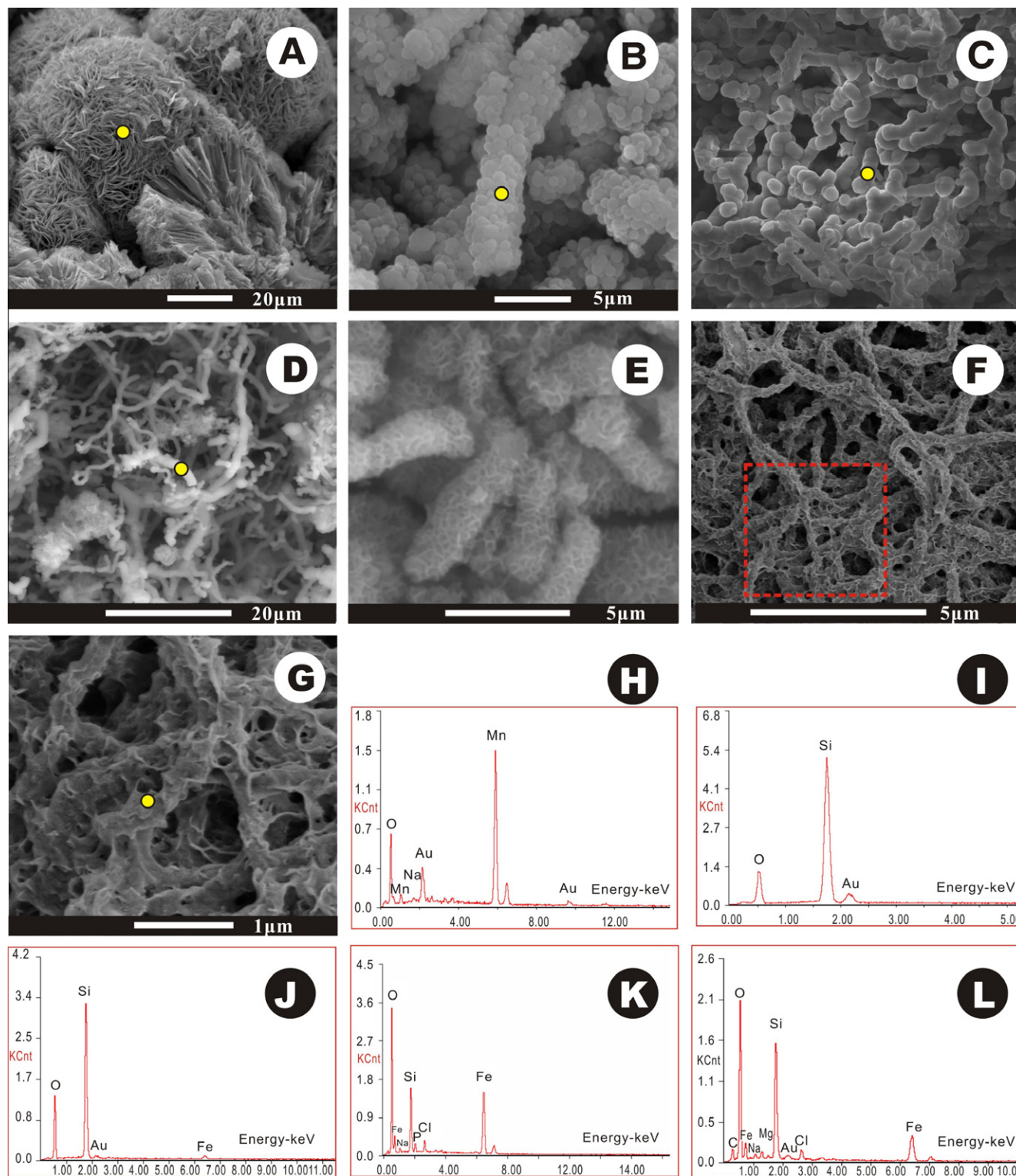


Fig. 6. SEM images (A, B, C, D, E, F, G) and corresponding EDS spectra (H, I, J, K, L) of hydrothermal Fe–Mn–Si oxides on the VFR. The yellow dots on the SEM photographs mark the EDS detection points. (A) Mn-oxide rosettes, sample L6B, the Hine Hina field; (B) amorphous opal globules completely coating the Fe-rich filaments, sample L9Y, the Mariner field; (C) filaments with short rod-like and oval appearances, sample L6Y, the Hine Hina field; (D) threadlike filaments in the Fe–Si–Mn deposits, sample L5Y, the Hine Hina field; (E) Patchy nontronite containing honeycomb-like cells, sample L9P, the Mariner field; (F) nontronite growing perpendicular to the surfaces of Fe–Si filament substrates, sample L5Y, the Hine Hina field; (G) close-up of the area in red framework of sub-figure F, showing a ragged nontronitic filament surface, sample L5Y, the Hine Hina field; (H) EDS spectrum of the rosette structure in sub-figure A; (I) EDS spectrum of the amorphous opal globules in sub-figure B; (J) EDS spectrum of the short rod-like structure in sub-figure C; (K) EDS spectrum of the thread-like structure in sub-figure D; (L): EDS spectrum of the ragged nontronitic filament surface in sub-figure G.

filaments shows that most of the filaments contain a threadlike “core” with higher Fe contents than the siliceous crust. The Fe-rich cores are up to 100 μm in length and 0.5–3 μm in diameter. It is

significant that there is no core in the globular or spheroidal structures. Typical SEM images and elemental analyses of Fe-rich cores are shown in Fig. 9. Our analytical results reveal that Fe

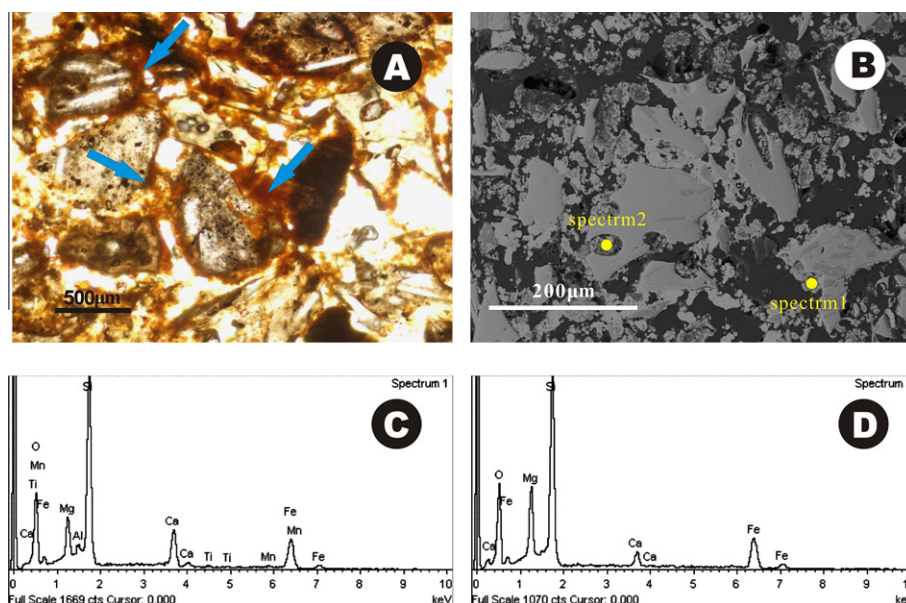


Fig. 7. (A) Photomicrographs of thin sections in plane polarized light showing the saponite rinds (as indicated by arrows) of altered basaltic debris, Sample from TVG6 station, the Hine Hina field; (B) SEM micrographs (secondary electron images) showing the EPMA detecting positions and the alteration rinds of basaltic debris. Sample from TVG6 station, the Hine Hina field; C, (D) corresponding EDS spectra of the altered rinds in sub-figure B.

and Si are the most important constituents in the filaments but that the enrichment of Fe is much stronger in the inner cores (9.5–29.1 wt.%) than in the outer crusts of the filaments (1.8–9.5 wt.%). Nonetheless, it should be noted that the Si contents are more abundant at every detection point than the Fe contents with the inner cores having a range of 28.7–41.0 wt.% Si and the outer crusts a range of 41.0–45.7 wt.% Si.

4.3. Precipitation temperatures

The $\delta^{18}\text{O}$ values of the four studied samples range from 16.1‰ to 32.1‰ (relative to VSMOW). The oxygen isotope ratio of nontronite purified from TVG5 (21.9‰; sample L5S) is significantly higher than that of the natural nontronite (16.1‰; sample L9P) but still falls within the range of other seafloor hydrothermal nontronites (Severmann et al., 2004). There is no significant isotopic difference between the two purified opal-A samples (32.1‰ and 31.7‰) but they are more isotopically positive than the nontronite samples. The oxygen isotope equilibration temperatures for nontronite-water were calculated using the equations $10^3 \ln \alpha_{\text{Nontronite-Water}} = 2.67(10^6 T^{-2}) - 4.82$ (Yeh and Savin, 1977) and $10^3 \ln \alpha_{\text{Opal-Water}} = 3.52(10^6 T^{-2}) - 4.35$ for opal-A-water (Kita et al., 1985). The mean $\delta^{18}\text{O}$ value of the hydrothermal fluids in the Mariner and Vai Lili hydrothermal fields is about 0.31‰ ($n = 7$; Mottl et al., 2011). According to this, the formation temperatures of these samples were calculated using the above equations and are presented in Table 3.

5. Discussion

5.1. Precipitation of hydrothermal biogenic Fe oxides

Within the redox boundary, there is always a competition between microbial and abiotic oxidation kinetics which begins when hydrothermal fluids invade the ambient seawater. Neutrophilic Fe-oxidizing bacteria function well and are adapted to take advantage of oxic–anoxic interfaces at this boundary (Brune et al., 2000; Emerson et al., 2010; Edwards et al., 2011). These bacteria can

grow on energy derived from the oxidation of Fe^{2+} to Fe^{3+} in order to fix CO_2 , a metabolism which is thought to lead to the precipitation of Fe oxyhydroxide (Kennedy et al., 2003b; Emerson et al., 2007, 2010). Based on the XRD and Mössbauer spectra results, ferrihydrite appears to be an important constituent of Fe–Mn–Si oxides despite the general occurrence of silicification in our samples. We also observed variants of stalks, sheaths, and other mineralized structures representing the neutrophilic Fe-oxidizing bacteria of *G. ferruginea*, *L. ochracea* and *M. ferrooxydans* in modern seafloor hydrothermal fields. Moreover, delicate textures in the biogenic mats (interlocking with each other to form meshes, Fig. 8G and H; radiation from a dense mass, Fig. 8I and J; orientation parallel to laminae Fig. 8K) in our samples were observed to form a complex network and create a unique niche which is crucial to Fe oxidizing bacteria because, in well oxygenated water, abiotic oxidation of Fe(II) is very rapid with a half-life of <1 min (Emerson et al., 2010). This requires the Fe oxidizing bacteria to grow under microaerobic conditions where the dissolved Fe(II) and O_2 concentrations are well controlled (Roden et al., 2004). In the Fe–Si oxide deposits of Lōihi Seamount, in situ voltammetric measurements of O_2 and dissolved Fe(II) show that oxygen is depleted at the mat surface and rapidly drops below detection limit (5 μM) within the first five cm whereas the Fe(II) was not detectable above the mat surface, but starting at the mat surface steadily increases with depth (Edwards et al., 2011). As a result, a microaerobic environment forms inside the mats in which neutrophilic Fe-oxidizing bacteria can outpace abiotic kinetics and thereby obtain enough energy to live (Emerson et al., 2010).

Our investigations also showed that tiny spheroidal blebs on the surface of the filaments are very common. This indicates that the individual bacterial sheaths and stalks could behave as a precipitation substrate for both oxidizing and oxidized iron. Actually, the autocatalytic oxidation of Fe(II) on Fe oxyhydroxide is an important sink for Fe(II). It can increase the rate of abiotic iron oxidation by nearly 10-fold and become another important source of competition for Fe(II). In addition, mineralized filaments in our samples commonly have much bigger sizes (hundreds of μm in length and several μm in diameter) than those of individual microbes (tens of μm in length and ca. 1 μm in diameter) even before

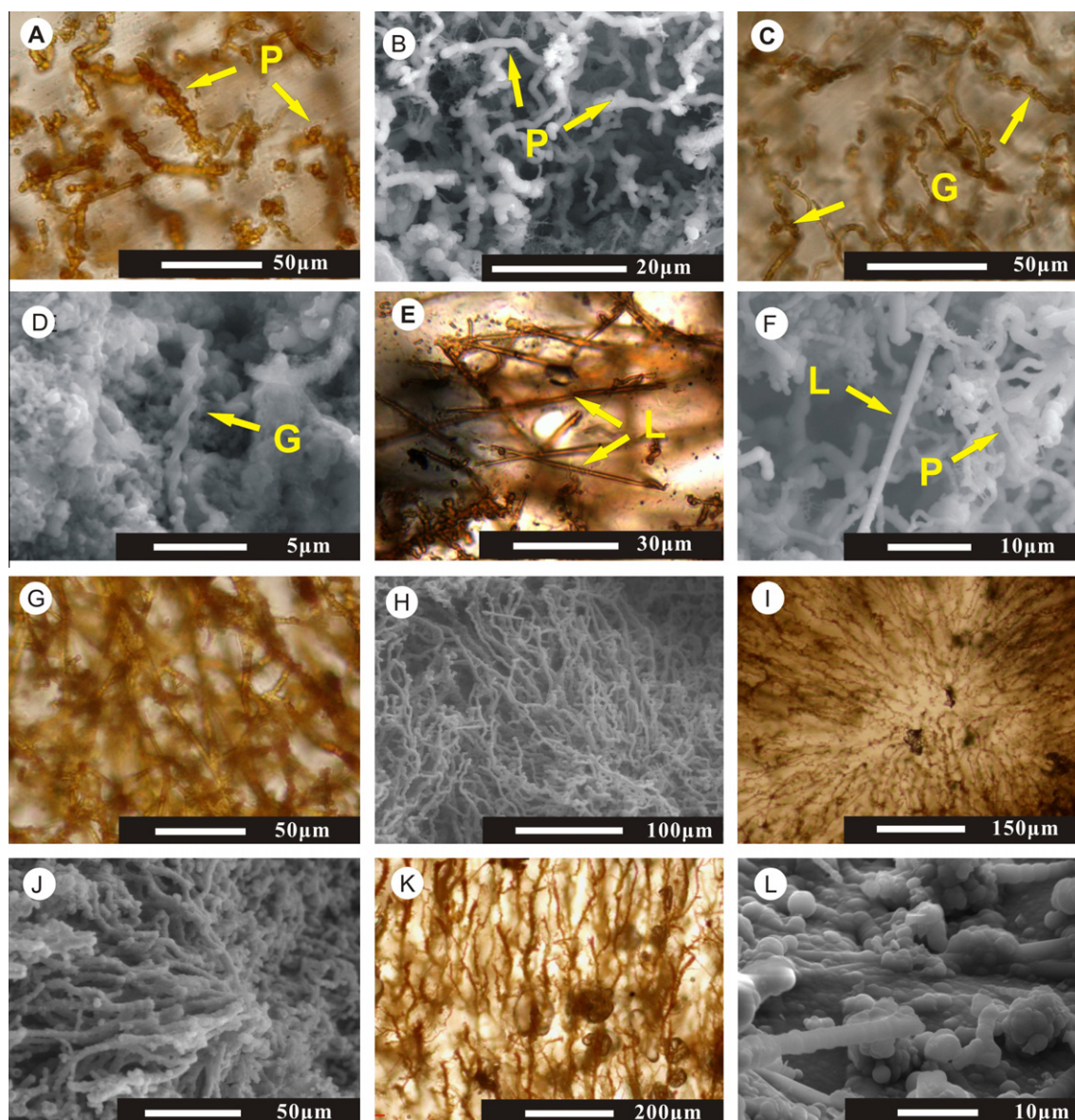


Fig. 8. Photomicrographs of Fe–Mn–Si oxides from the VFR in plane polarized light (thin sections) and SEM images. (A) morphology of individual filament resembling *Mariprofundus ferrooxydans* (abbreviated as “P”), note the precipitation of tiny Fe-containing spheres on the filament surface, sample L90; (B) SEM image of filaments resembling *Mariprofundus ferrooxydans* (abbreviated as “P”), sample L5Y; (C) mineralized twisted stalks of *Gallionella ferruginea* (abbreviated as “G”), sample L8Y; (D) SEM image of twisted stalks of *Gallionella ferruginea* (abbreviated as “G”), sample L5Y; (E) mineralized rod-like sheaths of *Leptothrix ochracea* (abbreviated as “L”) sample L6Y; (F) rod-like sheaths of *Leptothrix ochracea* (abbreviated as “L”) and filaments of *Mariprofundus ferrooxydans*, sample L5Y; (G) mesh-like structure formed by various filaments without a mineral cement in the voids, sample L6Y; (H) filamentous network constructed with mineralized filaments, sample L9Y; (I) mineralized filaments radiating out from a center, sample L8Y; (J) biogenic network composed of radial filaments, sample L8Y; (K) filaments oriented parallel to the laminae, sample L6Y; (L) biogenic filament network filled by opal-A as a result of later large-scale precipitation, sample L9Y.

silicification. This shows that, apart from intracellular mineralization, extracellular mineralization is characterized by an obvious increase in filament size after formation.

Although one should be cautious in judging members of iron-oxidizing bacteria based on morphological characteristics, a parallel study in molecular biology (Li, 2008) has confirmed our SEM and optical observations: two genes of neutrophilic Fe-oxidizing bacteria were recognized, one of which shares 94% of the 16S rRNA gene sequence to *G. ferruginea* (gene accession L07897) and the other 91% of the 16S rRNA gene sequence to *M. ferrooxydans* (PV-1 strain, gene accession EF493243). This confirms our observations on the morphologies and emphasizes the important role that neutrophilic Fe-oxidizing bacteria play in the formation of modern hydrothermal Fe–Mn–Si oxide deposits.

5.2. Precipitation of silica and mat silicification

Our studies show that general silicification has occurred in most Fe–Mn–Si oxide deposits in the Lau Basin. With respect to volume and content, amorphous opal dominates the composition of these samples. It is therefore critical to elucidate the process of Si precipitation for this study. Modern hydrothermal vent fluids are enriched in Si (the hydrothermal fluid of the Mariner field contains Si concentrations up to 15.2–15.6 mmol/kg; Takai et al., 2008) whereas seawater is depleted in Si relative to amorphous silica (bottom seawater contains 0.13 mmol/kg of Si in the Lau Basin; Mottl et al., 2011). As a consequence, the simple mixing of hydrothermal fluids with seawater does not result in supersaturation which begs the question of how silica in the hydrothermal fluid becomes saturated.

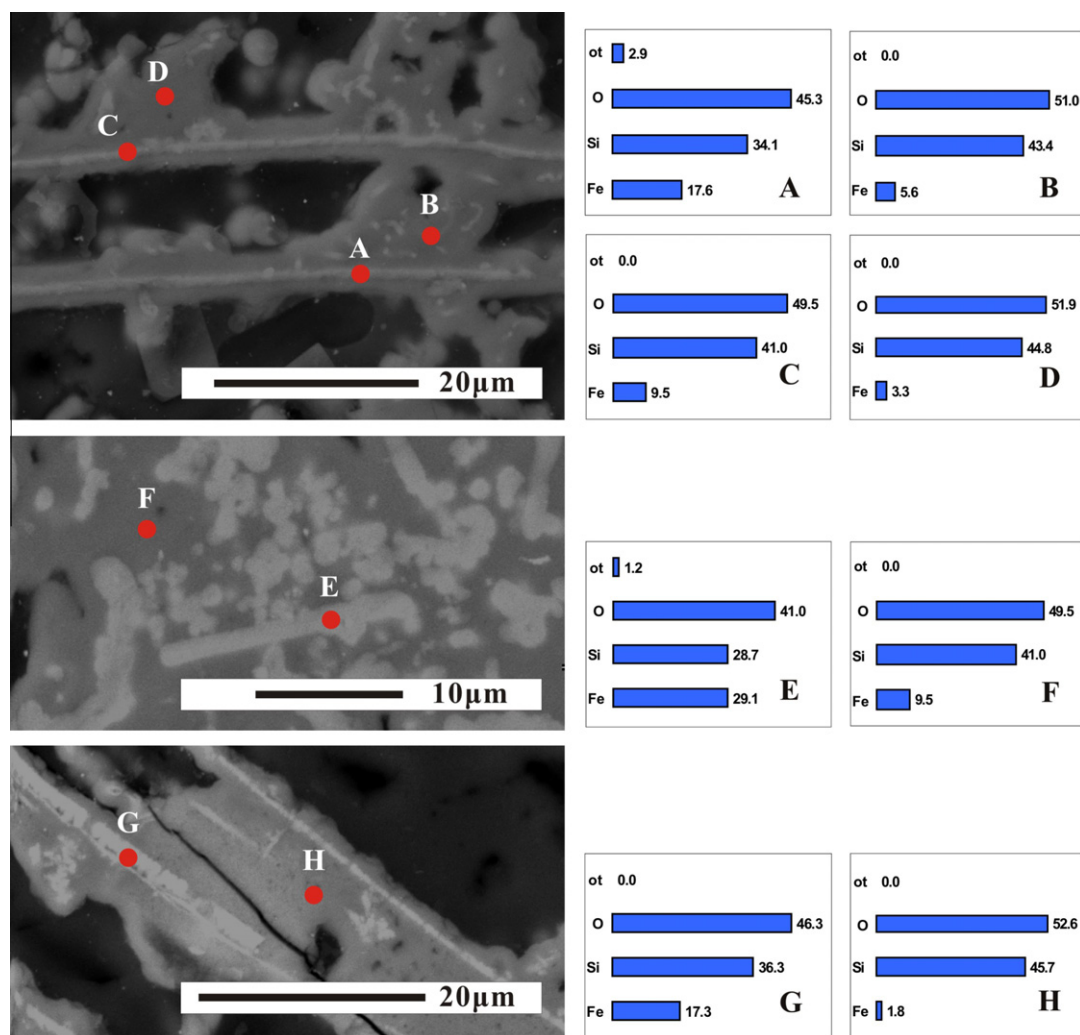


Fig. 9. SEM micrographs (secondary electron images) and EPMA analyses showing the composite structure of filaments in the hydrothermal Fe–Mn–Si oxide deposits on the VFR. The red solid circles mark the positions of the EPMA point analyses. The capital letters above the red circles are testing numbers consistent with the letters marked in the right histograms. These numbers show the mass percentage of each element. The “ot” represents the total percentage of the other elements (excluding Fe, Si and O) in these samples. The SEM photograph in the upper left is sample L5Y, the SEM photograph in the middle left is sample L8Y and the SEM photograph in the lower left is sample L9O.

Table 3

Oxygen isotopic composition and calculated formation temperatures for nontronite and opal-A on the VFR.

| Sample | Mineral types | $\delta^{18}\text{O}_{\text{V-SMOW}} (\text{‰})$ | T (°C) | Error in T (°C) ^a |
|--------|---------------------------------|--|--------|------------------------------|
| L5S | Nontronite (after purification) | 21.9 | 46.2 | ±0.6 |
| L9P | Nontronite (natural sample) | 16.1 | 87.9 | ±0.9 |
| L9O | opal-A (after purification) | 32.1 | 41.1 | ±0.7 |
| L9Y | opal-A (after purification) | 31.7 | 42.9 | ±0.6 |

^a Error represents experimental reproducibility between replicate determinations.

The precipitated silica in the filaments of our samples was split into two distinct generations. The first generation was silica within the iron-rich cores of the filaments. In these cores, the Si content is dominant (28.7–45.7 wt.%) despite the fact that Fe was more abundant in the cores relative to the crusts of the filaments. This indicates that a significant proportion of the silica co-precipitates with iron during the early stage of formation of the filaments. SEM and microscopic investigations reveal that the mats have not experienced widespread silicification and commonly contain abundant and relatively large meshes or pores. As a result, the

hydrothermal fluids and ambient seawater can mix freely in this stage. The silica is still unsaturated and does not precipitate in large quantities. Silica precipitation under these conditions appears to proceed under a process by which silica adsorbs onto ferrihydrite at circumneutral pH (Fein et al., 2002; Konhauser et al., 2004) and substitutes for double-cornered FeO_6 -octahedra in Fe oxyhydroxide polymeric complexes (Pokrovski et al., 2003). Microbes therefore play an indirect role in this process. Aqueous Si tends to be associated with bacterial surfaces, not as a result of direct interactions of Si with bacteria but rather because Si is highly reactive with Fe oxyhydroxides (ferrihydrite) which commonly precipitate and become associated with bacterial surfaces. As a result, Si can nucleate on the surface of the ferrihydrite which encrusts the microbe even when undersaturated with regard to opal-A (Juniper and Fouquet, 1988) and begins to precipitate, thereby forming the first generation of siliceous materials.

The second generation of silica occurs when the crust forms around an iron-rich core. This results in the enlargement of the size of filaments and a decrease in the permeability of the mat. The precipitation temperature of SiO_2 (41.1–42.9 °C) in these samples is higher than the optimum temperature for the growth of *G. ferruginea* and *M. ferrooxydans* (8–16 °C and 10–30 °C, respectively; Halbach et al., 2001; Emerson et al., 2007, 2010). This difference in

temperatures between the precipitation temperature of SiO₂ and the optimum temperature of the Fe-oxidizing bacteria manifests itself clearly during the mixing between the hydrothermal fluid and seawater, which was restricted and retarded when the second generation of silica begins to precipitate. Silica saturation then occurs inside the mats and is followed by large-scale opal-A precipitation (Juniper and Fouquet, 1988; Stüben et al., 1994). According to our studies, the second-generation silica in the filaments is thicker than the iron-rich core reflecting the more rapid precipitation rates compared to those of the first generation. Previous studies have implied that, when the saturated threshold value is reached, aqueous Si rapidly precipitates in the presence of ferrihydrite (Dyer et al., 2010). However, the relatively homogenous precipitation temperature of opal-A (41.1–42.9 °C) recorded in different samples in our study shows that silica precipitates in a narrow temperature range which confirms the fast precipitation rates of silica at this stage. The existence of non-core silica spheres in this generation suggests that abiotic factors control the kinetics of precipitation fully at this time. As a consequence, the Fe–Si filaments are wrapped in pure opal-A as a result of the constant precipitation of Si which fills the voids in the filament network. Following this, the density of the mats increases significantly and silicification ceases.

5.3. Formation of nontronite in hydrothermal fields

Nontronite precipitation tends to occur in conditions where the hydrothermal fluids have limited dilution in seawater at the optimum Eh range between –0.1 and –0.8 V (Köhler et al., 1994). Two parameters critical for the formation of nontronite rather than ferrihydrite or opal-A are relatively low Si concentrations and the presence of dissolved Fe(II) in the solution (Dekov et al., 2007). Additionally, the redox conditions must be kept stable for some time before the nontronite can precipitate. Precipitation of silicates therefore requires controlled cooling with minimal mixing in contrast to opal-A. In our deposits, paragenetic sequences from Fe–Si oxides to Mn oxides therefore reflect an oxidative trend whereas the presence of nontronite in Fe–Si–Mn oxides reflects the persistence of local reducing conditions.

The precipitation temperature of patchy nontronite in the Mariner field is 87.9 °C calculated by oxygen isotope data, which is higher than previously reported for the formation temperatures of authigenic nontronite (Severmann et al., 2004). This implies that the mixing between the hydrothermal fluid and seawater is relatively limited when the nontronite precipitates. The REE patterns of nontronite in this field (with a positive Eu anomaly, Eu/Eu* = 3.29 and no Ce anomaly, Ce/Ce* = 0.97, Sun et al., submitted for publication) are very similar to those of nontronite directly precipitated from hydrothermal fluids at the TAG field (Severmann et al., 2004) and is consistent with the formation of hydrothermal nontronite from other hydrothermal sites (Dekov et al., 2007). As mentioned above, the Mariner field is now in an active state and the occurrence of irregularly patchy nontronite probably indicates that limited mixing between hydrothermal fluids and seawater only occurs sporadically because of the pervasive invasion of hydrothermal fluids. This represents a mechanism for nontronite to form directly as hydrothermal precipitates in the vicinity of the active hydrothermal vent. However, it is fortuitous that the Fe³⁺ cations are split almost 1:1 (49.5:50.5%) between the M1 and M2 sites (Dyar et al., 2009). If this is not the limitation of the Lorentzian fit in estimating cis/trans site population ratios (Rancourt, 1994a,b), then the high distortion of these octahedral Fe microenvironments can be associated with the presence of large amounts of Al, Mg or even Mn cations (Dekov et al., 2007; Dyar et al., 2008). This relationship may reflect the complex composition of the hydrothermal fluid from which the nontronite precipitates in this area.

The calculated temperature of formation of nontronite in the Hine Hina field (46.2 °C) is lower than its counterpart in the Mariner field but is consistent with the formation temperature of the Fe–Si oxide (see table 3) and the hydrothermal diffuse flow temperature in the Hine Hina field (~40 °C; Fouquet et al., 1993; Lécuyer et al., 1999; Baker et al., 2005). Based on SEM observations (Fig. 6), the sparse honeycomb-like nontronites often grow perpendicular to the substrate of the Fe–Si oxides. This growth may indicate that the nontronites in this field were formed by replacement of hydrothermal Fe-oxides and inherit their formation temperatures. Cole (1985) reported a type of iron-rich smectite (nontronite) replacement of preformed siliceous microfossils in the Bauer Deep. He observed that biogenic opal and hydrothermal Fe oxide are the sources of nontronite in this area and these Fe–Si precipitates could be generated by co-precipitation of silica with Fe hydroxide under oxidizing conditions, which, if aged under reducing conditions, develop into crystalline nontronite. Our study has revealed that Fe–Si filaments generally act as substrates for authigenic nontronite formation in the Hine Hina field. Compared to the study of Cole (1985), the two generations of silica in these deposits could provide an abundant source of silica and the Fe(III) in the oxyhydroxide could be incorporated into solid siliceous crusts and result in the formation of nontronite. The ubiquitous nontronitic filaments in the Hine Hina hydrothermal field support this mechanism. This may therefore be another process for the formation of nontronite in these low temperature diffuse hydrothermal fields similar to that observed in some inactive hydrothermal fields (Severmann et al., 2004).

6. Conclusions

A variety of biogenic filaments is pervasive in the Fe–Mn–Si oxide precipitates recovered from hydrothermal fields in the VFR area, Lau Basin. SEM, EPMA and optical microscopy show that these deposits formed either as the result of direct metabolic activity of Fe-oxidizing bacteria or of the passive sorption and nucleation reactions on the surface of ferrihydrite encrusted microbes. The neutrophilic Fe-oxidizing bacteria such as *G. ferruginea*, *L. ochracea* and *M. ferrooxydans* are thought to be involved in this process based on our investigations. Two generations of silica were observed in these filaments. It is suggested that the first generation of silica is related to a significant portion of the Si that was adsorbed onto ferrihydrite encrustations on microbes under unsaturated conditions and that the second generation may be related to conductive cooling of the hydrothermal fluid inside the biogenic mats. These two generations of silica ultimately result in the rigorous silicification of the biogenic mats. The geochemistry and mineralogy of nontronite indicates the presence of two precipitation mechanisms for nontronite in the investigated hydrothermal fields. The patchy nontronite in the Mariner field is the result of direct precipitation of hydrothermal fluids at temperatures of about 87.9 °C whereas the scattered nontronite in the Hine Hina field is the result of replacement of hydrothermal Fe–Si oxides at a formation temperature of 46.2 °C.

Acknowledgements

This study was supported by the Natural Science Foundation of China (Project No. 40976045, 40976025 and 40976036). We gratefully thank Prof. Fuya Wang from Guangzhou Institute of Geochemistry (Chinese Academy of Sciences) for his analytical help with XRD and Dr. Sanyuan Zhu also from Guangzhou Institute of Geochemistry for his constructive suggestions and help in fitting the Mössbauer spectra. We also thank two anonymous reviewers for their thorough comments and constructive suggestions that helped to improve the manuscript.

References

- Alt, J.C., 1988. Hydrothermal oxide and nontronite deposits on seamounts in the eastern Pacific. *Marine Geology* 81, 227–239.
- Alt, J.C., Jiang, W.T., 1991. Hydrothermally precipitated mixed layer illite–smectite in recent massive sulphide deposits from the seafloor. *Geology* 19, 570–573.
- Baker, E.T., Massoth, G.J., Nakamura, K., Embley, R.W., de Ronde, C.E.J., Arculus, R.J., 2005. Hydrothermal activity on near-arc sections of back-arc ridges: results from the Mariana Trough and Lau Basin. *Geochemistry, Geophysics, Geosystems* 6, Q09001. doi:10.1029/2005GC000948.
- Baker, E.T., Resing, J.A., Walker, S.L., Martinez, F., Taylor, B., Nakamura, K., 2006. Abundant hydrothermal venting along melt-rich and melt-free ridge segments in the Lau back-arc basin. *Geophysical Research Letters* 33, L07308. doi:10.1029/2005GL025283.
- Benjamin, S.B., Haymon, R.M., 2006. Hydrothermal mineral deposits and fossil biota from a young (0.1 Ma) abyssal hill on the flank of the fast spreading East Pacific Rise: evidence for pulsed hydrothermal flow and tectonic tapping of axial heat and fluids. *Geochemistry, Geophysics, Geosystems* 7, Q05002. doi:10.1029/2005GC001011.
- Binns, R.A., Scott, S.D., Bogdanov, Y.A., Lisitzin, A.P., Gordeev, V.V., Gurvich, E.G., Finlayson, E.G., Boyd, T., Dotter, L.E., Wheller, G.E., Muravyev, K.G., 1993. Hydrothermal oxide and gold-rich sulfate deposits of Franklin Seamount, western Woodlark basin, Papua New Guinea. *Economic Geology* 88, 2122–2153.
- Boyce, A.J., Little, C.T.S., Russell, M.J., 2003. A new fossil vent biota in the Ballynoe Barite Deposit, Silvermines, Ireland: evidence for intracratonic sea-floor hydrothermal activity about 352 Ma. *Economic Geology* 98, 649–656.
- Boyd, T.D., Scott, S.D., 2001. Microbial and hydrothermal aspects of ferric oxyhydroxides and ferrous hydroxides: the example of Franklin Seamount, Western Woodlark Basin, Papua New Guinea. *Geochemical Transactions* 2, 45 (5 September 2001).
- Brune, A., Frenzel, P., Cypionka, H., 2000. Life at the oxic–anoxic interface: microbial activities and adaptations. *FEMS Microbiology Reviews* 24, 691–710.
- Chan, C.S., Fakra, S.C., Emerson, D., Fleming, E.J., Edwards, K.J., 2011. Lithotrophic iron-oxidizing bacteria produce organic stalks to control mineral growth: implications for biosignature formation. *The ISME Journal* 5, 717–727.
- Clayton, R.N., Mayeda, T.K., 1963. The use of bromine pentafluoride in the extraction of oxygen in oxides and silicates for isotopic analysis. *Geochimica et Cosmochimica Acta* 27, 43–52.
- Coffin, D.E., 1963. A method for the determination of free iron in soils and clays. *Canadian Journal of Soil Science* 43, 9–17.
- Cole, T.G., 1983. Oxygen isotope geothermometry and origin of smectites in the Atlantis II Deep, Red Sea. *Earth and Planetary Science Letters* 66, 166–176.
- Cole, T.G., 1985. Composition, oxygen isotope geochemistry, and origin of smectite in the metalliferous sediments of the Bauer Deep, southeast Pacific. *Geochimica et Cosmochimica Acta* 49, 221–235.
- Cole, T.G., 1988. The nature and origin of smectite in the Atlantis II Deep, Red Sea. *Canadian Mineralogist* 26, 755–763.
- Cole, T.G., Shaw, H.F., 1983. The nature and origin of authigenic smectites in some recent marine sediments. *Clay minerals* 18, 239–252.
- Davis, R., Moyer, C., 2008. Extreme spatial and temporal variability of hydrothermal microbial mat communities along the Mariana island arc and southern Mariana backarc system. *Journal of Geophysical Research* 113, B08S15.
- Dekov, V.M., Kamenov, G.D., Stummeyer, J., Thiry, M., Savelli, C., Shanks, W.C., Fortin, D., Kuzmann, E., Vértés, A., 2007. Hydrothermal nontronite formation at Eolo Seamount (Aeolian volcanic arc Tyrrhenian Sea). *Chemical Geology* 245, 103–119.
- Dekov, V.M., Petersen, S., Garbe-Schönberg, C.-D., Kamenov, G.D., Perner, M., Kuzmann, E., Schmidt, M., 2010. Fe–Si-oxyhydroxide deposits at a slow-spreading centre with thickened oceanic crust: The Lilliput hydrothermal field (9°33′S, Mid-Atlantic Ridge). *Chemical Geology* 278, 186–200.
- Dhillon, A., Teske, A., Dillon, J., Stahl, D.A., Sogin, M.L., 2003. Molecular characterization of sulfate-reducing bacteria in the Guaymas Basin. *Applied and Environmental Microbiology* 69, 2765–2772.
- Duhig, N.C., Stolz, J., Davidson, C.J., Large, R.R., 1992. Cambrian microbial and silica gel textures in silica iron exhalites from the Mount Windsor Volcanic Belt, Australia: their petrography, chemistry, and origin. *Economic Geology* 87, 764–784.
- Dyar, M.D., Schaefer, M.W., Sklute, E.C., Bishop, J.L., 2008. Mössbauer spectroscopy of phyllosilicates: effects of fitting models on recoil-free fractions and redox ratios. *Clay Minerals* 43, 3–33.
- Dyar, M.D., Sklute, E.C., Menzies, O.N., Bland, P.A., Lindsley, D., Glotch, T., Lane, M.D., Schaefer, M.W., Wopenka, B., Klima, R., Bishop, J.L., Hiroi, T., Pieters, C., Sunshine, J., 2009. Spectroscopic characteristics of synthetic olivine: an integrated multi-wavelength and multi-technique approach. *American Mineralogist* 94, 883–898.
- Dyer, L., Fawell, P.D., Newman, O.M.G., Richmond, W.R., 2010. Synthesis and characterisation of ferrihydrite/silica co-precipitates. *Journal of Colloid and Interface Science* 348, 65–70.
- Edwards, K.J., Glazer, B.T., Rouxel, O.J., Bach, W., Emerson, D., Davis, R.E., Toner, B.M., Chan, C.S., Tebo, B.M., Staudigel, H., Moyer, C.L., 2011. Ultra-diffuse hydrothermal venting supports Fe-oxidizing bacteria and massive amber deposition at 5000m off Hawaii. *The ISME Journal*. doi:10.1038/ismej.2011.48.
- Emerson, D., Moyer, C.L., 2002. Neutrophilic Fe-oxidizing bacteria are abundant at the Loihi Seamount hydrothermal vents and play a major role in Fe oxide deposition. *Applied and Environmental Microbiology* 68, 3085–3093.
- Emerson, D., Rentz, J.A., Lilburn, T.G., Davis, R.E., Aldrich, H., Chan, C., Moyer, C.L., 2007. A novel lineage of proteobacteria involved in formation of marine Fe-oxidizing microbial mat communities. *PLoS one* 2 (7), 667. doi:10.1371/journal.pone.0000667.
- Emerson, D., Fleming, E.J., McBeth, J.M., 2010. Iron-oxidizing bacteria: an environmental and genomic perspective. *Annu. Rev. Microbiol.* 64, 561–583.
- Fein, J.B., Scott, S., Rivera, N., 2002. The effect of Fe on Si adsorption by *Bacillus subtilis* cell walls: insights into non-metabolic bacterial precipitation of silicate minerals. *Chemical Geology* 182, 265–273.
- Fortin, D., Ferris, F.G., Scott, S.D., 1998. Formation of Fe-silicates and Fe-oxides on bacterial surfaces in hydrothermal deposits collected near the Southern Explorer Ridge in the Northeast Pacific Ocean. *American Mineralogist* 83, 1399–1408.
- Fouquet, Y., von Stackelberg, U., Charlou, J.L., Donval, J.P., Foucher, J.P., Erzinger, J., Herzig, P., Mühe, R., Wiedicke, M., Soakai, S., Whitechurch, H., 1991. Hydrothermal activity in the Lau back-arc basin: sulfides and water chemistry. *Geology* 19, 303–306.
- Fouquet, Y., von Stackelberg, U., Charlou, J.L., Donval, J.L., Erzinger, J., Foucher, J.P., Herzig, P., Mühe, R., Soakai, S., Wiedicke, M., 1993. Metallogenesis in back-arc environments: the Lau Basin example. *Economic Geology* 88, 2154–2181.
- Halbach, M., Koschinsky, A., Halbach, P., 2001. Report on the discovery of *Gallionella ferruginea* from an active hydrothermal field in the deep sea. *InterRidge News* 10, 18–20.
- Hawkins, J.W., 1995. Evolution of the Lau Basin: insights from ODP Leg 135. In: Taylor, B., Natland, J. (Eds.), *Active Margins and Marginal Basins of the Western Pacific*, vol. 88. AGU Geophysical Monograph, pp. 125–173.
- Haymon, R.M., Kastner, M., 1986. The formation of high temperature clay minerals from basalt alteration during hydrothermal discharge on the East Pacific Rise axis at 21°N. *Geochimica et Cosmochimica Acta* 50, 1933–1939.
- Hekinian, R., Hoffer, M., Larqué, P., Cheminée, J.L., Stoffers, P., Bideau, D., 1993. Hydrothermal Fe and Si oxyhydroxide deposits from South Pacific intraplate volcanoes and East Pacific Rise axial and off-axial regions. *Economic Geology* 88, 2099–2121.
- Herzig, P.M., Becker, K.P., Stoffers, P., Bäcker, H., 1988. Hydrothermal silica chimney fields in the Galapagos Spreading Center at 86°W. *Earth and Planetary Science Letters* 89, 261–272.
- Hodges, W., Olson, J.B., 2009. Molecular comparison of bacterial communities within iron-containing flocculent mats associated with submarine volcanoes along the Kermadec Arc. *Applied and Environmental Microbiology* 75, 1650–1657.
- Hofmann, B.A., Farmer, J.D., Von Blanckenburg, F., Fallick, A., 2008. Subsurface filamentous fabrics: an evaluation of origins based on morphological and geochemical criteria, with implications for exopaleontology. *Astrobiology* 8, 87–117.
- Hrischeva, E., Scott, S.D., 2007. Geochemistry and morphology of metalliferous sediments and oxyhydroxides from the Endeavour segment, Juan de Fuca Ridge. *Geochimica et Cosmochimica Acta* 71, 3476–3497.
- Iizasa, K., Kawasaki, K., Maeda, K., Matsumoto, T., Saito, N., Hirai, K., 1998. Hydrothermal sulfide-bearing Fe–Si oxyhydroxide deposits from the Coriolis Troughs, Vanuatu backarc, southwestern Pacific. *Marine Geology* 145, 1–21.
- Ishibashi, J., Lupton, J.E., Yamaguchi, T., Querellou, J., Nunoura, T., Takai, K., 2006. Expedition reveals changes in Lau Basin hydrothermal system. *EOS, Transactions American Geophysical Union* 87, 13–17.
- Jackson, M.L., 1985. *Soil Chemical Analysis – Advanced Course*, 2nd ed., 11th printing, published by the author, Madison, WIS 53705.
- Jambor, J.L., Dutrizac, J.E., 1998. Occurrence and constitution of natural and synthetic ferrihydrite, a widespread iron oxyhydroxide. *Chemical Reviews* 98, 2549–2585.
- Jenner, G.A., Cawood, P.A., Rautenschlein, M., White, W.M., 1987. Composition of back-arc basin volcanics, Valu Fa Ridge, Lau Basin: evidence for a slab-derived component in their mantle source. *Journal of Volcanology and Geothermal Research* 32, 209–222.
- Jones, J.B., Segnit, F.R., 1971. The nature of opal 1. Nomenclature and consistent phases. *Journal of the Geological Society of Australia* 18, 57–68.
- Jones, J.B., Segnit, F.R., 1975. Nomenclature and the structure of natural disordered (opaline) silica. *Contributions to Mineralogy and Petrology* 51, 231–234.
- Juniper, S.K., Fouquet, Y., 1988. Filamentous iron–silica deposits from modern and ancient hydrothermal sites. *Canadian Mineralogist* 26, 859–869.
- Kato, S., Kobayashi, C., Kakegawa, T., Yamagishi, A., 2009. Microbial communities in iron–silica-rich microbial mats at deep-sea hydrothermal fields of the Southern Mariana Trough. *Environmental Microbiology* 11, 2094–2111.
- Keller, N.S., Arculus, R.J., Hermann, J., Richards, S., 2008. Submarine back-arc lava with arc signature: Fonualei Spreading Center, northeast Lau Basin, Tonga. *Journal of Geophysical Research* 113, B08S07. doi:10.1029/2007JB005451.
- Kennedy, C.B., Martinez, R.E., Scott, S.D., Ferris, F.G., 2003a. Surface chemistry and reactivity of bacteriogenic iron oxides from Axial Volcano, Juan de Fuca Ridge, north-east Pacific Ocean. *Geobiology* 1, 59–69.
- Kennedy, C.B., Scott, S.D., Ferris, F.G., 2003b. Characterization of bacteriogenic iron oxide deposits from Axial Volcano, Juan de Fuca Ridge, north-east Pacific Ocean. *Geomicrobiology Journal* 20, 199–214.
- Kita, I., Taguchi, S., Matsubaya, O., 1985. Oxygen isotope fractionation between amorphous silica and water at 34–93 °C. *Nature* 314, 83–84.
- Köhler, B., Singer, A., Stoffers, P., 1994. Biogenic nontronite from marine white smoker chimneys. *Clay and Clay Minerals* 42, 689–701.
- Konhauser, K.O., Jones, B., Phoenix, V.R., Ferris, G., Renaut, R.W., 2004. The microbial role in hot spring silicification. *Ambio* 33, 552–558.

- Langley, S., Igric, P., Takahashi, Y., Sakai, Y., Fortin, D., Hannington, M.D., Schwarz-Schampera, U., 2009. Preliminary characterization and biological reduction of putative biogenic iron oxides (BIOs) from the Tonga-Kermadec Arc, southwest Pacific Ocean. *Geobiology* 7, 35–49.
- Lécuyer, C., Dubois, M., Marignac, C., Gruau, G., Fouquet, Y., Ramboz, C., 1999. Phase separation and fluid mixing in subseafloor back arc hydrothermal systems: a microthermometric and oxygen isotope study of fluid inclusions in the barite-sulfide chimneys of the Lau basin. *Journal of Geophysical Research* 104 (B8), 17911–17927.
- Li, J., 2008. Study on the Microbial Diversity of Deep-sea Hydrothermal Chimney and Microbial Mineralization. Ph. D. Thesis, Graduate School of the Chinese Academy of Sciences, Beijing, pp. 151–172.
- Little, C.T.S., Glynn, S.E.J., Mills, R.A., 2004. Four-hundred and ninety-million-year record of bacteriogenic iron oxide precipitation at sea-floor hydrothermal vents. *Geomicrobiology Journal* 21, 415–429.
- Martinez, F., Taylor, B., Baker, E.T., Resing, J.A., Walker, S.L., 2006. Opposing trends in crustal thickness and spreading rate along the backarc Eastern Lau Spreading Center: implications for controls on ridge morphology, faulting, and hydrothermal activity. *Earth and Planetary Science Letters* 245, 655–672.
- McMurtry, G.M., Yeh, H.-W., 1981. Hydrothermal clay mineral formation of East Pacific Rise and Bauer Basin sediments. *Chemical Geology* 32, 189–205.
- McMurtry, G.M., Wang, C.-H., Yeh, H.-W., 1983. Chemical and isotopic investigations into the origin of clay minerals from the Galapagos hydrothermal mounds field. *Geochimica et Cosmochimica Acta* 47, 475–489.
- Mikutta, C., Mikutta, R., Bonneville, S., Wagner, F., Voegelin, A., Christl, I., Kretzschmar, R., 2008. Synthetic coprecipitates of exopolysaccharides and ferrihydrite. Part I: characterization. *Geochimica et Cosmochimica Acta* 72, 1111–1127.
- Mottl, M.J., Seewald, J.S., Wheat, C.G., Tivey, M.K., Michael, P.J., Proskurowski, G., McCollom, T.M., Reeves, E., Sharkey, Jessica, You, C.-F., Chan, L.-H., Pichler, T., 2011. Chemistry of hot springs along the Eastern Lau Spreading Center. *Geochimica et Cosmochimica Acta* 75, 1012–1038.
- Murad, E., Schwertmann, U., 1980. The Mössbauer spectrum of ferrihydrite and its relations to those of other iron oxides. *American Mineralogist* 65, 1044–1049.
- Pansu, M., Gautheryrou, J., 2006. *Handbook of Soil Analysis: Mineralogical, Organic and Inorganic Methods*. Springer-Verlag, Berlin, pp. 26–49.
- Pecoits, E., Gingras, M.K., Barley, M.E., Kappler, A., Posth, N.R., Konhauser, K.O., 2009. Petrography and geochemistry of the Dales Gorge banded iron formation: Paragenetic sequence, source and implications for palaeo-ocean chemistry. *Precambrian Research* 172, 163–187.
- Percival, J.B., Ames, D.E., 1993. Clay mineralogy of active hydrothermal chimneys and associated mound, Middle Valley, Northern Juan de Fuca Ridge. *Canadian Mineralogist* 31, 957–971.
- Pokrovski, G.S., Schott, J., Farges, F., Hazemann, J.-L., 2003. Iron (III)-silica interactions in aqueous solution: Insights from X-ray absorption fine structure spectroscopy. *Geochimica et Cosmochimica Acta* 67, 3559–3573.
- Puteanus, D., Glasby, G.P., Stoffers, P., Kunzendorf, H., 1991. Hydrothermal iron-rich deposits from the Teahitia-Mehitia and Macdonald hot spot areas, Southwest Pacific. *Marine Geology* 98, 389–409.
- Rancourt, D.G., 1994a. Mössbauer spectroscopy of minerals I. Inadequacy of Lorentzian-line doublets in fitting spectra arising from quadrupole splitting distributions. *Physics and Chemistry of Minerals* 21, 244–249.
- Rancourt, D.G., 1994b. Mössbauer spectroscopy of minerals II. Problem of resolving cis and trans octahedral Fe²⁺ sites. *Physics and Chemistry of Minerals* 21, 250–257.
- Rancourt, D.G., Fortin, D., Pichler, T., Thibault, P.-J., Lamarche, G., Morris, R.V., Mercier, P.H.J., 2001. Mineralogy of a natural As-rich hydrous ferric oxide coprecipitate formed by mixing of hydrothermal fluid and sea water: Implications regarding surface complexation and color banding in ferrihydrite deposits. *American Mineralogist* 86, 834–851.
- Reysenbach, A.-L., Liu, Y., Banta, A.B., Beveridge, T.J., Kirshtein, J.D., Schouten, S., Tivey, M.K., Von Damm, K.L., Voytek, M.A., 2006. A ubiquitous thermoacidophilic archaeon from deep-sea hydrothermal vents. *Nature* 442, 444–447.
- Roden, E.E., Sobolev, D., Glazer, B., Luther, G.W.I., 2004. Potential for microscale bacterial Fe redox cycling at the aerobic-anaerobic interface. *Geomicrobiology Journal* 21, 379–391.
- Severmann, S., Mills, R.A., Palmer, M.R., Fallick, A.E., 2004. The origin of clay minerals in active and relict hydrothermal deposits. *Geochimica et Cosmochimica Acta* 68, 73–88.
- Sherman, D.M., Vergo, N., 1988. Optical (diffuse reflectance) and Mossbauer spectroscopic study of nontronite and related Fe-bearing smectites. *American Mineralogist* 73, 1346–1354.
- Stüben, D., Eddine, T.N., McMurtry, G.M., Scholten, J., Stoffers, P., Zhang, D., 1994. Growth history of a hydrothermal silica chimney from the Mariana backarc spreading center (southwest Pacific, 18°13'N). *Chemical Geology* 113, 273–296.
- Sun, Z., Zhou, H., Glasby, G.P., Sun, Z., Yin, X., Li, J., submitted for publication. Mineralogical characterization and formation of Fe-Si oxyhydroxide deposits from modern seafloor hydrothermal vents. *American Mineralogist*.
- Taitel-Goldman, N., Singer, A., 2001a. High-resolution transmission electron microscopy study of newly formed sediments in the Atlantis II Deep, Red Sea. *Clays and Clay Minerals* 49, 174–182.
- Taitel-Goldman, N., Singer, A., 2001b. Metastable Si-Fe phases in hydrothermal sediments of Atlantis II Deep, Red Sea. *Clay Minerals* 37, 235–248.
- Takai, K., Nunoura, T., Ishibashi, J., Lupton, J., Suzuki, R., Hamasaki, H., Ueno, Y., Kawagucci, S., Gamo, T., Suzuki, Y., Hirayama, H., Horikoshi, K., 2008. Variability in the microbial communities and hydrothermal fluid chemistry at the newly discovered Mariner hydrothermal field, southern Lau Basin. *Journal of Geophysical Research* 113, G02031. doi:10.1029/2007JG000636.
- Taylor, B., Zellmer, K., Martinez, F., Goodliffe, A., 1996. Sea-floor spreading in the Lau back-arc basin. *Earth and Planetary Science Letters* 144, 35–40.
- Taylor, C.D., Wirsén, C.O., Gaill, F., 1999. Rapid microbial production of filamentous sulfur mats at hydrothermal vents. *Applied and Environmental Microbiology* 65, 2253–2255.
- Wilson, M.J., 1987. Soil smectites and related interstratified minerals: recent developments. In: Shultz, L.G., Oiphen, H.V., Mumpton, F.A. (Eds.), *Proceedings of International Clay Conference*, Denver, Colorado, 1985. Clay Mineral Society, Bloomington, Indiana, USA, pp. 167–173.
- Yeh, H.W., Savin, S.M., 1977. Mechanism of burial metamorphism of argillaceous sediments: 3. O-isotope evidence. *Geological Society of America Bulletin* 88, 1321–1330.
- Zee, C., Slomp, C.P., Rancourt, D.G., Lange, G.J., Raaphorst, W., 2005. A Mössbauer spectroscopic study of the iron redox transition in eastern Mediterranean sediments. *Geochimica et Cosmochimica Acta* 69, 441–453.